Tag Surface Reconstruction and Tracking of Myocardial Beads from SPAMM-MRI with Parametric B-Spline Surfaces

Amir A. Amini*, *Senior Member, IEEE*, Yasheng Chen, Mohamed Elayyadi, and Petia Radeva

***Abstract*—Magnetic resonance imaging (MRI) is unique in its ability to noninvasively and selectively alter tissue magnetization, and create tag planes intersecting image slices. The resulting grid of signal voids allows for tracking deformations of tissues in otherwise homogeneous-signal myocardial regions. In this paper, we propose a specific spatial modulation of magnetization (SPAMM) imaging protocol together with efficient techniques for measurement of three-dimensional (3-D) motion of material points of the human heart (referred to as myocardial beads) from images collected with the SPAMM method. The techniques make use of tagged images in orthogonal views by explicitly reconstructing 3-D B-spline surface representation of tag planes (tag planes in two orthogonal orientations intersecting the short-axis (SA) image slices and tag planes in an orientation orthogonal to the short-axis tag planes intersecting long-axis (LA) image slices). The developed methods allow for viewing deformations of 3-D tag surfaces, spatial correspondence of long-axis and short-axis image slice and tag positions, as well as nonrigid movement of myocardial beads as a function of time.**

***Index Terms*—B-spline surfaces, cardiac motion, myocardial beads, myocardial infarction, tagged MRI.**

I. Introduction

NONINVASIVE techniques for assessing the dynamic behavior of the human heart are invaluable in the diagnosis of heart disease, as abnormalities in the myocardial motion sensitively reflect deficits in blood perfusion [20]. Magnetic resonance imaging (MRI) is a noninvasive imaging technique that provides superb anatomic information with excellent spatial resolution and soft tissue contrast. Conventional MR studies of the heart provide accurate measures of global myocardial function, chamber volumes and ejection fractions, and regional wall motions and thickening. In MR tagging, the magnetization property of selective material points in the myocardium are altered in order to create tagged patterns within a deforming body such as the heart muscle. The resulting pattern defines a time-varying curvilinear coordinate system on the tissue. During tissue contractions, the grid patterns move, allowing for visual tracking of the grid intersections over time. The intrinsic high spatial and temporal resolutions of such myocardial analysis schemes provide unsurpassed information about local contraction and deformation in the heart wall which can be used to derive local strain and deformation indices from different myocardial regions.

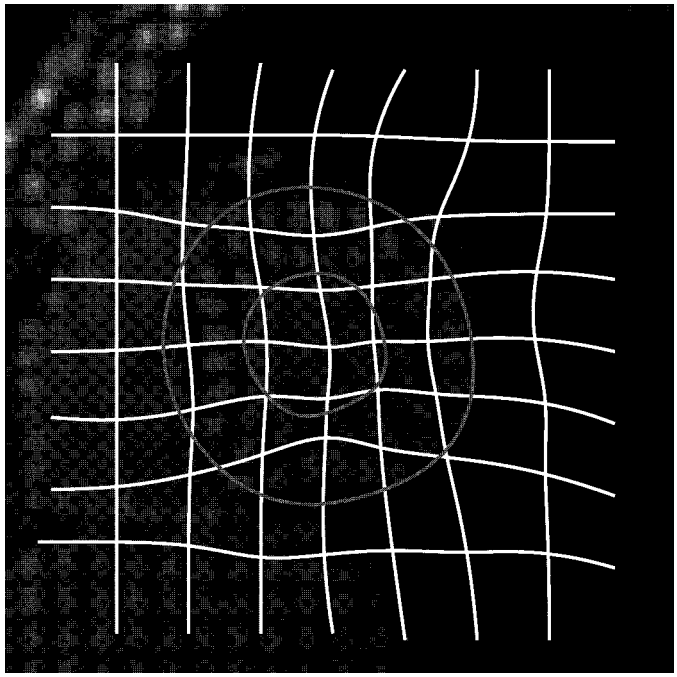

Fig. 1. A grid of B-spline snakes on short-axis image slices in mid-systole. Note that for better illustration, in this figure every second tag line is displayed. The analysis area of interest is the region within the myocardial borders of the LV.

Previous work for analysis of tagged images includes [19] who adopted an analysis system for tagged images based on snakes. Once the tag positions on the myocardium are found, coordinates of these points in deformed images are determined within a volumetric finite element model fitted to endocardial and epicardial contours. In [16], geometric primitives which are generalization of volumetric ellipsoids are considered and parameter functions are used which allow for spatial variations of aspect ratios of the model along the long axis of the left-ventricle (LV). This model is specially useful for computing the twisting motion of the heart. Optical flow-based approaches to the analysis of tagged MR images were proposed in [9]. The

Manuscript received November 17, 1998; revised November 10, 2000. This work is supported in part by a grant from Whitaker Biomedical Engineering Foundation, and Grants HL57628 and HL64217 from the National Institutes of Health. The Associate Editor responsible for coordinating the review of this paper and recommending its publication was J. S. Duncan. *Asterisk indicates corresponding author.*

*A. A. Amini is with the Cardiovascular Image Analysis Lab., Campus Box 8086, 660 S. Euclid Ave., Washington University Medical Center, St. Louis, MO 63110-1093 USA (e-mail: amini@mobius.wustl.edu, www: http://www-cv.wustl.edu).

Y. Chen, M. Elayyadi, and P. Radeva are with the CVIA Lab., Washington University Medical Center, St. Louis, MO 63110-1093 USA.

Publisher Item Identifier S 0278-0062(01)01309-X.

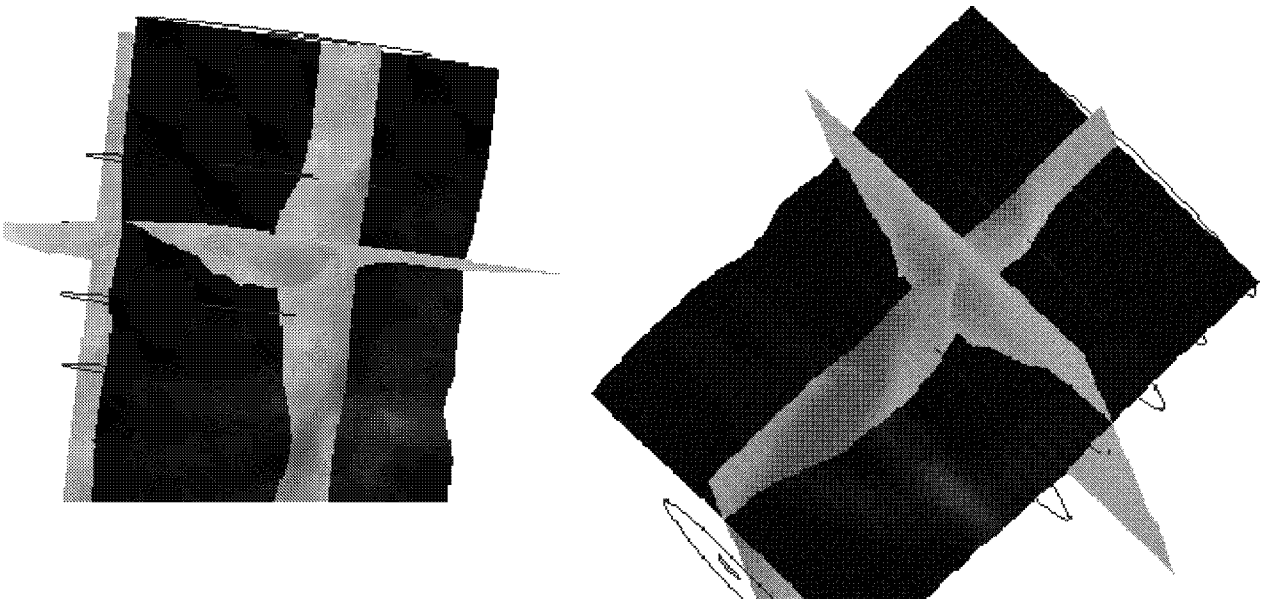

Fig. 2. Reconstruction of two orthogonal tag surfaces from a sequence of coupled B-spline curves in short-axis image slices (as in Fig. 1). Two views of the same tag planes are shown. The dark surface corresponds to the second vertical grid line from the right in Fig. 1. The bright vertical surface orthogonal to this surface corresponds to the fourth horizontal grid line from the top. Finally, the bright horizontal surface is the long-axis tag plane corresponding to the short-axis image slice. The compute time for generating this display was under one second on a Sun Ultra 30/300 MHz workstation.

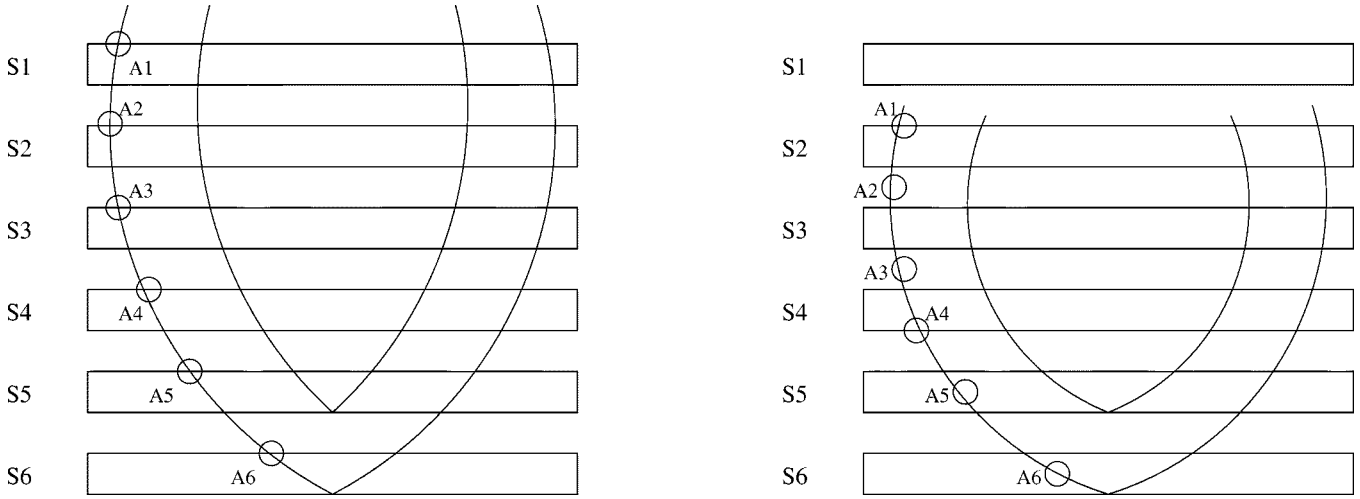

Fig. 3. Imaging geometry in MRI. The position of slices $(S1, \ldots, S6)$ are fixed relative to the magnet's coordinate system. However, a dynamic organ such as the heart moves in-and-out of the slices. Motion of points $A1, \ldots, A6$ illustrates this.

approach in [10] for analysis of radial tagged images uses a graph-search technique that determines the optimal inner and outer boundaries of the myocardium as well as tag lines by finding points one after the other in a sequence, using initial search starting points on the determined LV boundaries. In [1], [2], and [3], tag lines are tracked with dynamic programming B-snakes and coupled B-snake grids. Spline warps then warp an area in the plane such that snake grids obtained from two SPAMM frames are brought into registration, interpolating a dense displacement vector field. A volumetric B-solid model was proposed in [17] to concurrently analyze and track tag lines in different image slices by implicitly defined B-spline surfaces which align themselves with tagged data. The solid is a three-dimensional (3-D) tensor product B-spline whose isoparametric curves deform under image forces from tag lines in different image slices. In [12], tag surfaces were constructed using thin-plate splines, and subsequently intersection of the thin-plate spline surfaces were computed based on an alternating projection algorithm to yield displacements of myocardial beads.

Although the latter two articles provide novel techniques for computation of tag surfaces from discrete image slices, the former paper ([17]) cannot reconstruct tag surfaces independent of a B-solid. The latter article ([12]) leads to a somewhat compute intensive algorithm for tag surface reconstruction; in particular requiring inversion of the thin-plate spline matrix [7] of order $O(n \times n)$ (n being the total number of tag points on all image slices.) Assuming 30 samples per tag curve and seven image slices, it is not difficult to see that n can approach upwards of 200. Furthermore, intersecting thin-plate spline surfaces has to be performed in the Euclidean space since the surfaces are not of parametric form. The present article pro-

vides machinery for very fast computation of tag surfaces using B-snakes on individual slices in under one second, does not require *a priori* computation of a solid, and furthermore since by design the surfaces are parametric, it leads to a naturally easy to implement algorithm for computing the position of 3-D myocardial beads.

II. Reconstruction of Tag Planes from Coupled B-Snake Grids

B-splines are suitable for representing a variety of industrial and anatomical shapes [1], [2], [4], [5], [8], [11], [13]–[15]. The advantages of B-spline representations are: 1) They are smooth, continuous parametric curves which can represent open or closed curves. For our application, due to parametric continuity, B-splines will allow for subpixel localization of tags, 2) B-splines are completely specified by few control points, and 3) Individual movement of control points will only affect their shape locally. In medical imaging, local tissue deformations can easily be captured by movement of individual control points without affecting static portions of the curve.

A B-spline curve (of order k) is expressed as

$$\vec{\alpha}(u) = \sum_{i=0}^{N-1} \vec{V}_i B_{i,k}(u) \tag{1}$$

where $B_{i,k}(u)$ are the B-spline basis functions having polynomial form, and local support, and $\vec{V}_i$ are the sequence of control point of the B-spline curve. Two remarks should be made regarding the sequence of control points: a) The number of control points is much fewer in number than a sampling of the curve $\vec{\alpha}(u)$ on a pixel grid and b) $\vec{V}_i$ rarely reside on the actual curve. To localize a tag line based on B-snakes, an external energy can be defined and optimized in order to locate feature points on individual image slices [1], [2], [17]. Given a spatial stack of m curves on m image slices, each represented by n control points, a matrix of control points is constructed as follows:

$$\begin{bmatrix} \vec{V}_{11} & \cdots & \vec{V}_{1n} \\ & \cdots & \\ \vec{V}_{m1} & \cdots & \vec{V}_{mn} \end{bmatrix} \tag{2}$$

where the first index denotes ordering of control points across image slices along the z axis, and the second index denotes ordering of control points along the curve—within the image slice. The matrix immediately gives rise to the surface (of order k)

$$\vec{S}(u,v) = \sum_i \sum_j \vec{V}_{ij} B_{i,k}(u) B_{j,k}(v) \tag{3}$$

where we have used nonperiodic blending functions with t_i's as the knot sequence [15]

$$B_{i,k}(u) = \frac{(u - t_i) B_{i,k-1}(u)}{t_{i+k-1} - t_i} + \frac{(t_{i+k} - u) B_{i+1,k-1}(u)}{t_{i+k} - t_{i+1}} \tag{4}$$

We have applied cubic splines (i.e., $k = 4$) to ensure that the necessary flexibility exists in the parametrized shapes. Furthermore, given that tag lines and images are of approximately equal distance, uniform B-splines are considered so that the knots are spaced at consecutive integer values of parametric variables.

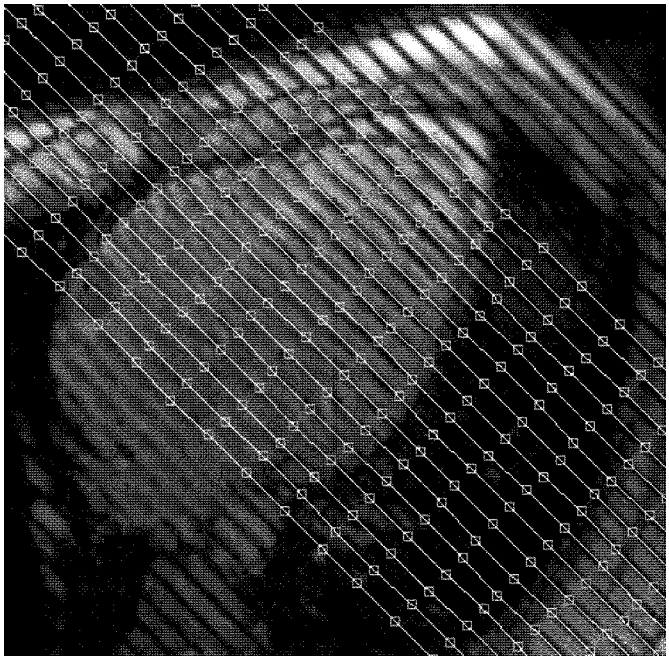

Fig. 4. Position of short-axis image slices at the time of tag placement is drawn on a long-axis image acquired at the same time point in the heart cycle.

TABLE I
Description of the 13 k Parameters

k_1	*Radially dependent compression*
k_2	*Left ventricular torsion*
k_3	*Ellipticalization in long axis planes*
k_4	*Ellipticalization in short axis planes*
k_5	*Shear in x direction*
k_6	*Shear in y direction*
k_7	*Shear in z direction*
k_8	*Rotation about $x-axis$*
k_9	*Rotation about $y-axis$*
k_{10}	*Rotation about $z-axis$*
k_{11}	*Translation in x direction*
k_{12}	*Translation in y direction*
k_{13}	*Translation in z direction*

Figs. 1 and 2 illustrate the construction of intersecting cubic B-spline tag surfaces from a spatial stack of coupled B-snake grids.

III. Nonrigid Tracking

The procedure outlined in Section II provides a mechanism for tracking points within short-axis image slices. However, as shown in Fig. 3, in MRI, position of image slices are fixed relative to the magnet's coordinate system and, therefore, this approach can only yield within short-axis-slice motion of material points. To obtain information about movement of points in the "out-of-plane" direction, a second sequence of images is acquired with slices parallel to the heart's long-axis and with the requirement that tag planes intersecting the new slices be in parallel to short axis images.

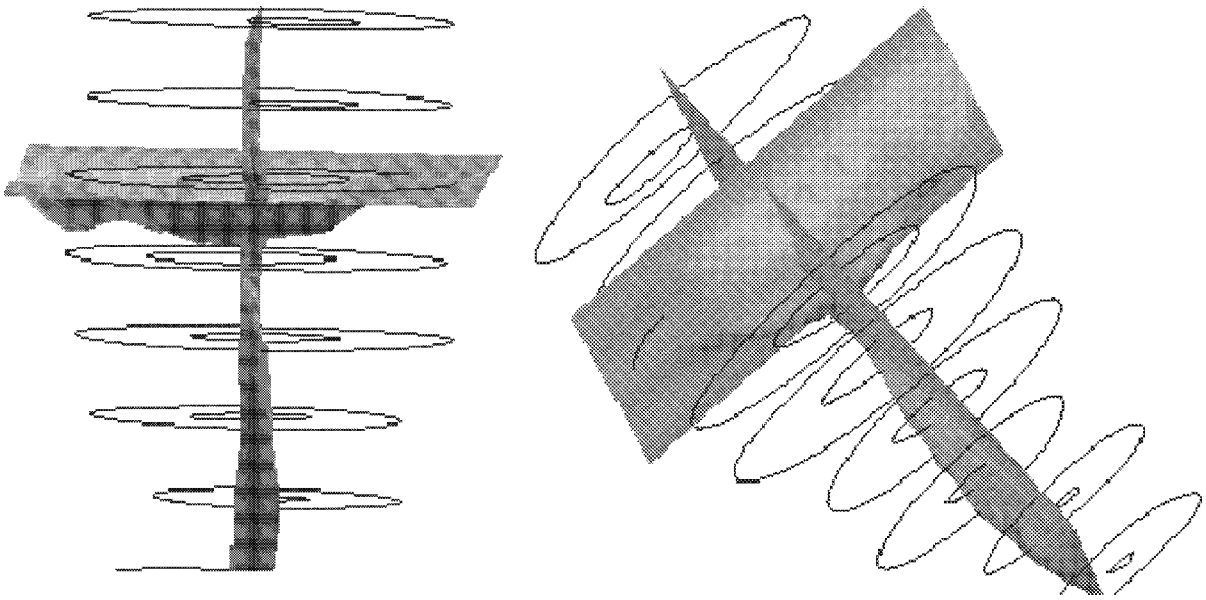

Fig. 5. B-spline surface representation of a long-axis tag plane reconstructed from a spatial stack of B-snakes. Two views of a reconstructed long-axis tag surface is displayed horizontally. "Out-of-plane" movement of the heart is visualized by deviation from flatness of the long-axis B-spline surface. The compute time for generating this display was under one second on a Sun Ultra 30/300 MHz workstation.

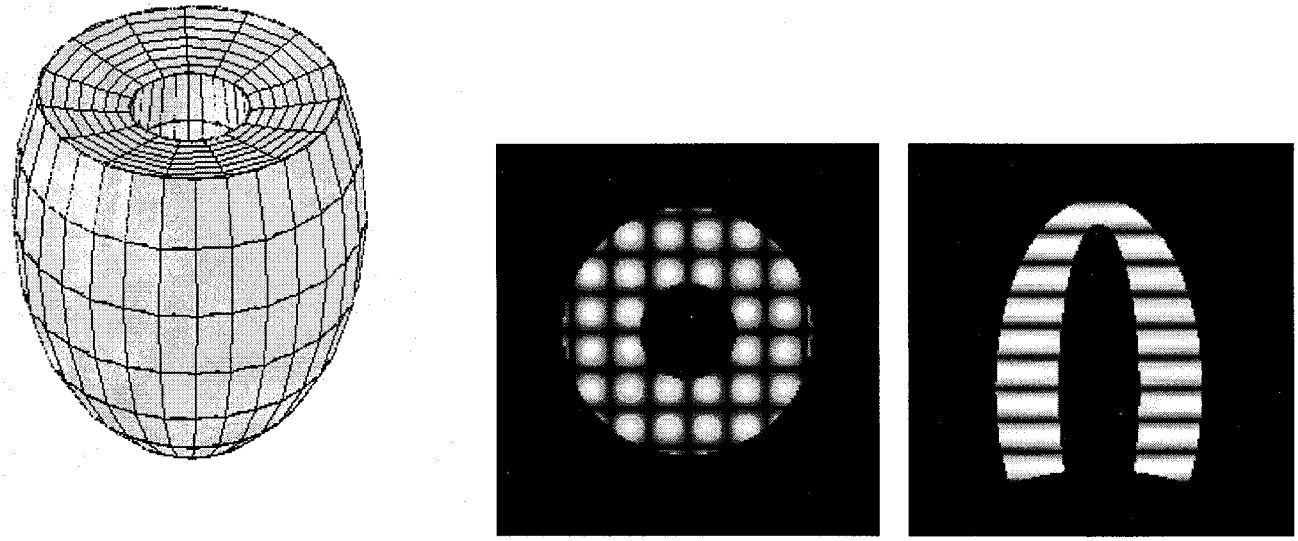

Fig. 6. The undeformed prolate spheroidal model of the LV in the reference state. A tagged image corresponding to a selected SA imaging plane at $z = 0.785$ cm and a LA imaging plane at $y = 0$ cm are shown on the right. The width of the "donut" is about 1.5 cm, and the discretization step is 0.05 cm. See Table II for the imaging parameters and dimensions of the geometric model.

A. Imaging Protocol

A breath-hold SPAMM pulse sequence was used to collect multiple images in both short-axis and long-axis views of the entire heart without gaps. Immediately after the electrocardiogram (ECG) trigger, radio-frequency (RF) tagging pulses were applied in two orthogonal directions. The repetition time (TR) of the imaging sequence was approximately 7.1 ms, the echo time (TE) was 2.9 ms, the RF pulse flip angle was 15°, and the time extent of RF tag pulses was 2.2 ms. Echo sharing was used in collecting each time-varying image sequence for given slice position. Five data lines were collected for any time frame during each heart cycle, but two data lines were overlapped between two consecutive cardiac frames, resulting in an effective temporal resolution of approximately 22 ms. Other imaging parameters were: field of view $= 330$ mm, data acquisition matrix size $= 160 \times 256$ (phase encoding by readout), in-plane resolution $= 2.1 \times 1.3$ mm^2, slice thickness $= 7$ mm, and tag spacing $= 7$ mm.

The image orientations for the short-axis and long-axis views of the heart were first determined by collecting multiple oblique angle scout images. For the short-axis images, one of the tagging planes was placed parallel to the long-axis imaging planes of the heart by manually setting the angles of the tagging plane in the coordinate system of the magnet to be the same as those of the long-axis view as determined from scout images. The coordinates of the center of the central tagging plane in the reference coordinates system (relative to the center of the magnet)

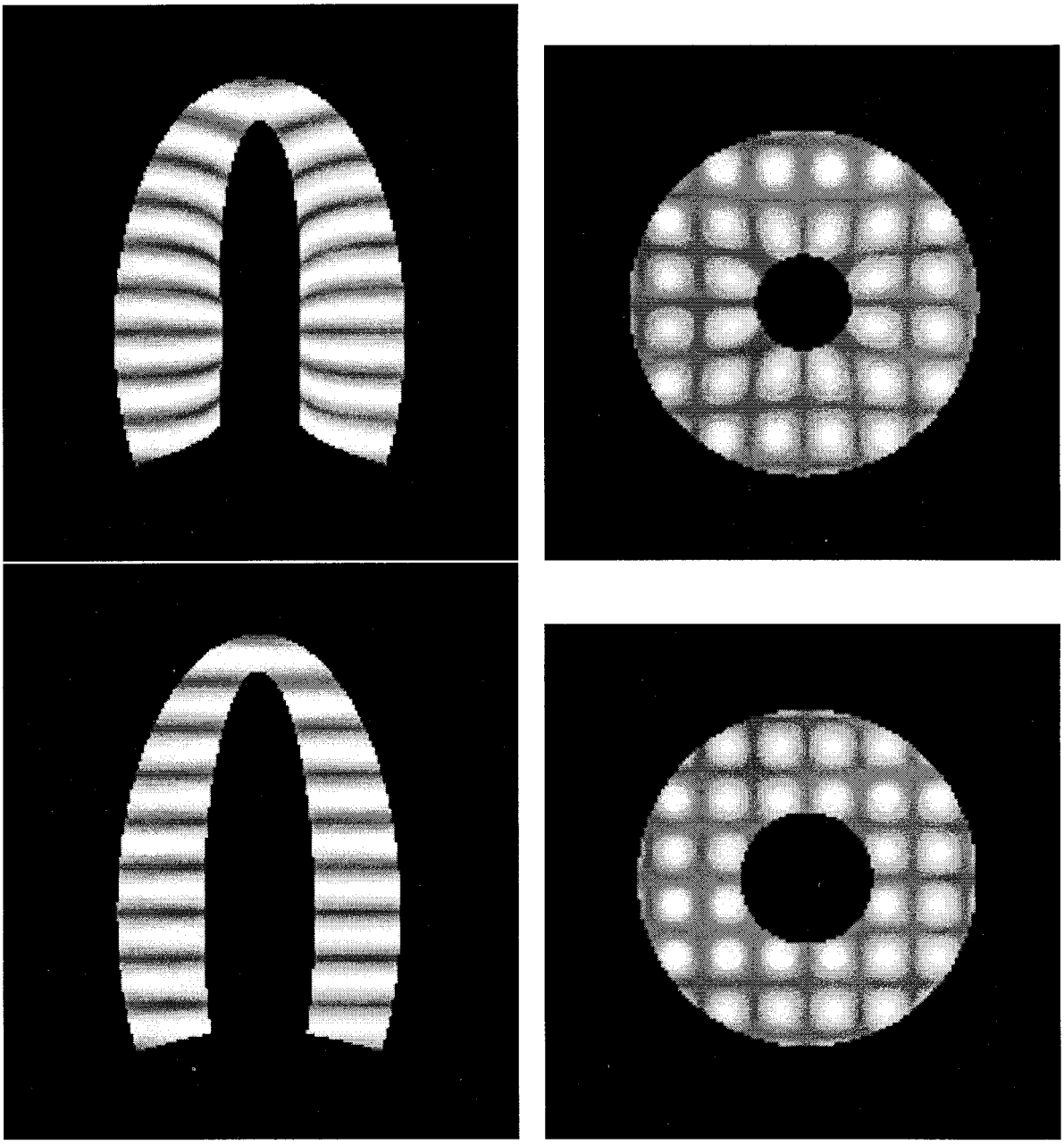

Fig. 7. Simulated SA and LA images corresponding to changing k_1 from 0 to -0.1 (top) (left: $y = 0$ cm, right: $z = 0.785$ cm), and k_3 to 0.045 from 0 (bottom) (left: $y = -0.785$ cm, right: $z = 0.785$ cm). See Table II for the imaging parameters and dimensions of the geometric model.

TABLE II
IMAGING PARAMETERS AND DIMENSIONS OF GEOMETRIC MODEL USED TO GENERATE SA AND LA IMAGES FOR FIGS. 6, 7, 8, 9, AND 11. PLEASE NOTE THAT TS IS TAG SEPARATION, R_i AND R_o ARE THE INNER AND OUTER RADII OF THE TWO PROLATE SPHEROIDS, AND ss IS THE SAMPLE SIZE

TS	D_0	TE	TR	$T1$	$T2$	k_x	k_y	θ	R_i	R_o	δ	ss
0.785 cm	300	0.03 sec	10 sec	0.6 sec	0.1 sec	8 rad/cm	8 rad/cm	45 deg.	0.25	0.6	4 cm	0.05 cm/pixel

were set to be the same as those of the center of one of the long-axis image planes to be acquired, again determined by the scout images. As a result, one set of tagging planes intersecting short-axis image slices coincided with long-axis images since both tag spacing and slice thickness were 7 mm center-to-center. The other short-axis tagging plane was placed orthogonal to the first tagging plane. Similarly, long-axis images were acquired with their tag planes coinciding with short-axis slice positions. It should be noted, however, that these requirements are not stringent. Indeed, the method described in Section III-B will continue to apply as long as three sequences of intersecting tag planes are encoded within the LV myocardium. However, the fact that at end-diastole, long-axis tag planes coincide with short-axis image slice locations and one set of short-axis tag

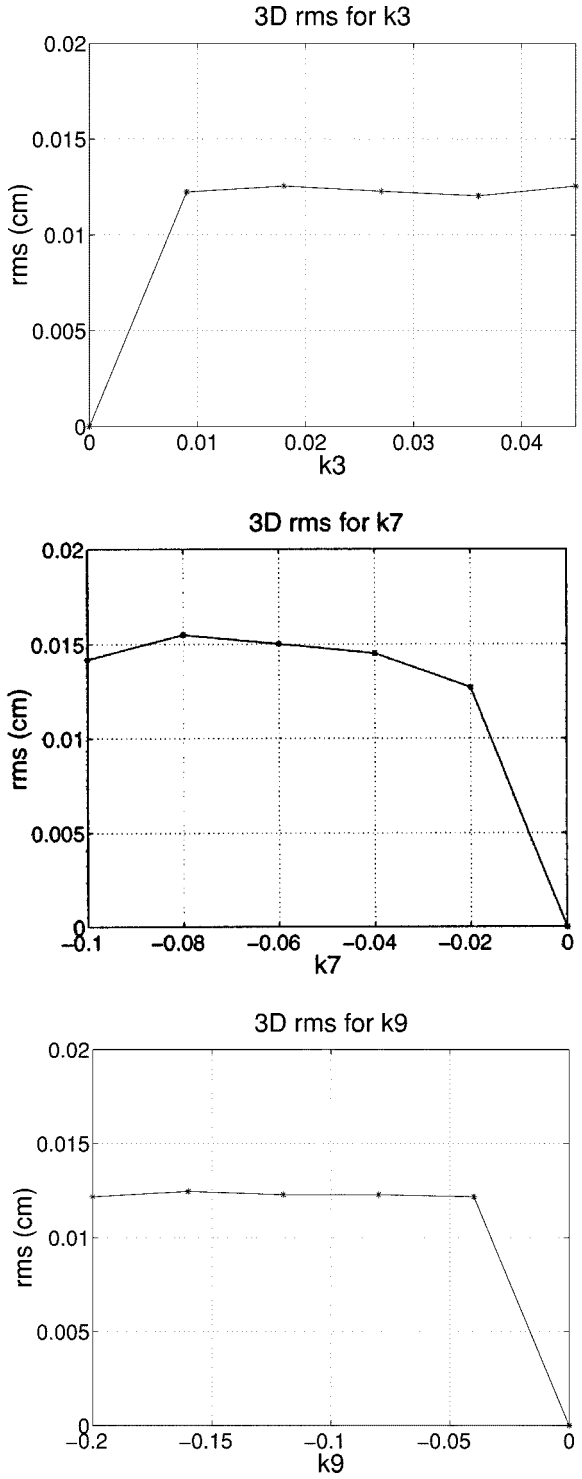

Fig. 8. RMS error plots [see, (7)] as a function of k_3, k_7, and k_9. To generate these error curves, the deformation matrix [18], was directly applied to the locations of tag line control points in the undeformed reference state. Intersections of the triplet of tag surfaces were then found and the rms error between computed, and theoretical intersections were calculated. In all cases, $k_i = 0$ represents the undeformed reference state at time 0. Note that in the above plots, depending on whether k_i increases or decreases from zero, time increases from left to right, or right to left. See Table II for the imaging parameters and dimensions of the geometric model.

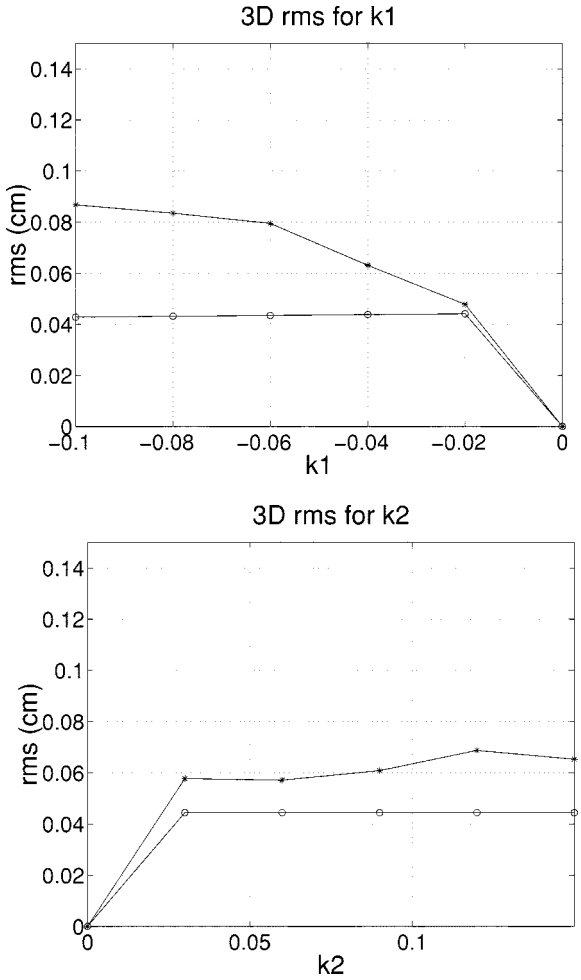

Fig. 9. RMS error plots for all the simulated myocardial beads as a function of k_1 and k_2 with tag detection and manual correction. In all cases, $k_i = 0$ represents the undeformed reference state at time 0. For the k_1 plot, time increases from right to left and for k_2 plot time increases from left to right. In each case, the top plot represents the rms error with tag spacing of 0.785 cm and the bottom plot is the error curve with tag spacing of 0.393 cm. See Table II for the imaging parameters and dimensions of the geometric model.

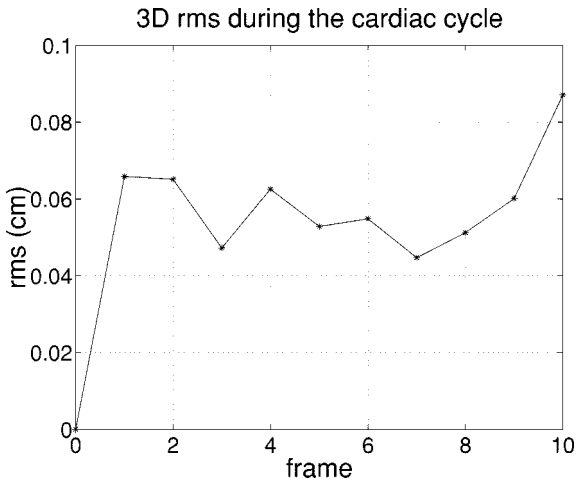

Fig. 10. RMS error plots for all the simulated myocardial beads during the whole cardiac cycle when all the k parameters are concurrently varied. The k parameters for each time point were found by least-squares fitting to an *in-vivo* canine heart over the entire ECG cycle [6]. See Table III for the imaging parameters and dimensions of the geometric model.

planes coincides with long-axis image slice locations leads to an interesting byproduct, namely, that location of myocardial tag lines on SA and LA images at end-diastole can simply be read

TABLE III
IMAGING PARAMETERS AND DIMENSIONS OF GEOMETRIC MODEL USED TO GENERATE SA AND LA IMAGES FOR FIG. 10. PLEASE NOTE THAT TS IS TAG SEPARATION, R_i AND R_o ARE THE INNER AND OUTER RADII OF THE TWO PROLATE SPHEROIDS, AND ss IS THE SAMPLE SIZE

TS	D_0	TE	TR	$T1$	$T2$	k_x	k_y	θ	R_i	R_o	δ	ss
0.785 cm	300	0.03 sec	10 sec	0.6 sec	0.1 sec	8 rad/cm	8 rad/cm	45 deg.	0.35	0.6	4 cm	0.05 cm/pixel

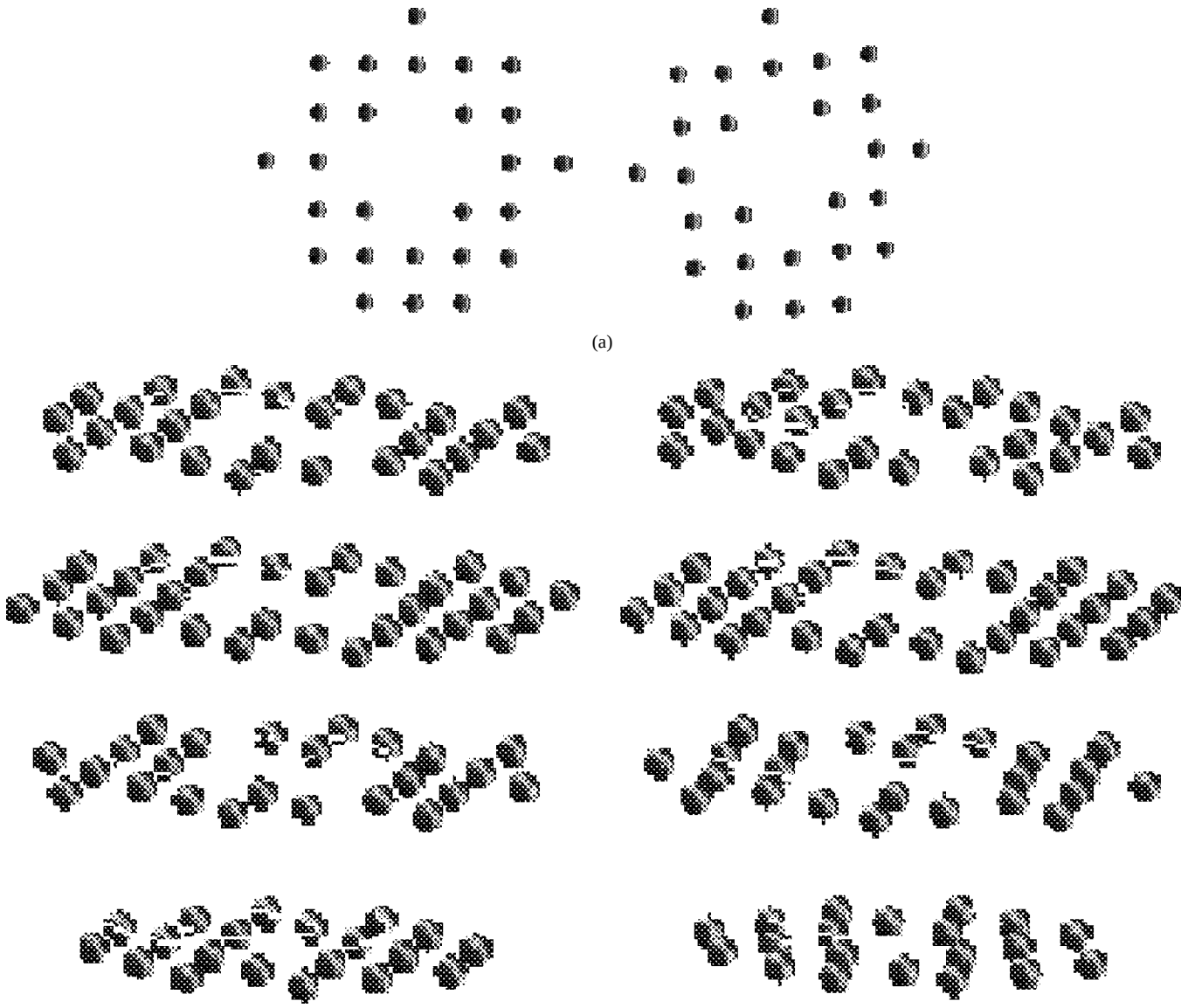

(a)

(b)

Fig. 11. Intersections computed for the k_2 sequence. (a) Slice 0 of the spatial stack at times 0 ($k_2 = 0$) and 5 ($k_2 = 0.15$). (b) Slices 0, 2, 4, and 6 at times 0 and 5. For a quicktime movie, visit http://www-cv.wustl.edu/demos/index.html. See Table II for the imaging parameters and dimensions of the geometric model.

off from image headers. To illustrate, Fig. 4 displays position of the short-axis image slices on one long-axis image at end-diastole.

As a result of the imaging protocol outlined in this section, the tag intersections are the myocardial beads corresponding precisely to the intersection of three tag planes, and revealing for all time points in the cardiac cycle, 3-D motion of these special points.

B. Computing Time-Dependent Coordinates of Myocardial Beads

As we did in the case of coupled B-snakes of short-axis images, once again we measure deformations of tag planes in the long-axis orientation by creating B-spline surfaces from stacks of B-snakes. The difference between short-axis and long-axis image acquisitions, however, is that there is only one set of parallel tag planes intersecting long-axis images. Fig. 5 illustrates a tag surface constructed from a spatial sequence of long-axis images.

Coordinates of myocardial beads may be obtained by computing intersections of three intersecting B-spline surfaces representing three intersecting tag surfaces. For each triplet of intersecting B-spline surfaces, $(\vec{S}_1(u_1, v_1), \vec{S}_2(u_2, v_2), \vec{S}_3(u_3, v_3))$, the following computation is performed:

$$\min_{\vec{P}_1, \vec{P}_2, \vec{P}_3} d^2(\vec{S}_1, \vec{S}_2) + d^2(\vec{S}_1, \vec{S}_3) + d^2(\vec{S}_2, \vec{S}_3) \qquad (5)$$

Fig. 12. (a) Initial 3-D location of myocardial beads at end-diastole on every second slice of the MRI data for a normal human volunteer. (b) Location of the beads for every fourth slice of the MRI data for the same time. (c) Computed location of the same points one-third through systole. Nonrigid motion of the heart can be appreciated: points further up in slices (around the base) move downwards, whereas points near the heart's apex are relatively stationary. Also, note that beads outside the LV wall remain static.

where point $\vec{P}_i$ belongs to surface $\vec{S}_i$ and d is the Euclidean distance metric. The minimization is carried out using the method of Conjugate Gradient Descent which ensures fast convergence of the method. Note that the overall distance function above can be written as

$$||\vec{S}_1(u_1,v_1)-\vec{S}_2(u_2,v_2)||^2+||\vec{S}_2(u_2,v_2)-\vec{S}_3(u_3,v_3)||^2 + ||\vec{S}_1(u_1,v_1)-\vec{S}_3(u_3,v_3)||^2 \quad (6)$$

with the goal of finding the parameters (u_i, v_i) for the triplet of surfaces. The computed parameters will in fact be surface parameters of the intersection point. For the iterative optimization process, a good initial set of parameters has been found to be parameters of the intersection point assuming linear B-spline bases.

IV. Validations

In order to validate the accuracy of the methods in measuring 3-D motion of myocardial points, the 13-parameter kinematic model of Arts *et al.* [6] as described in [18] was adopted. The simulator is capable of generating MR images at arbitrary ori-

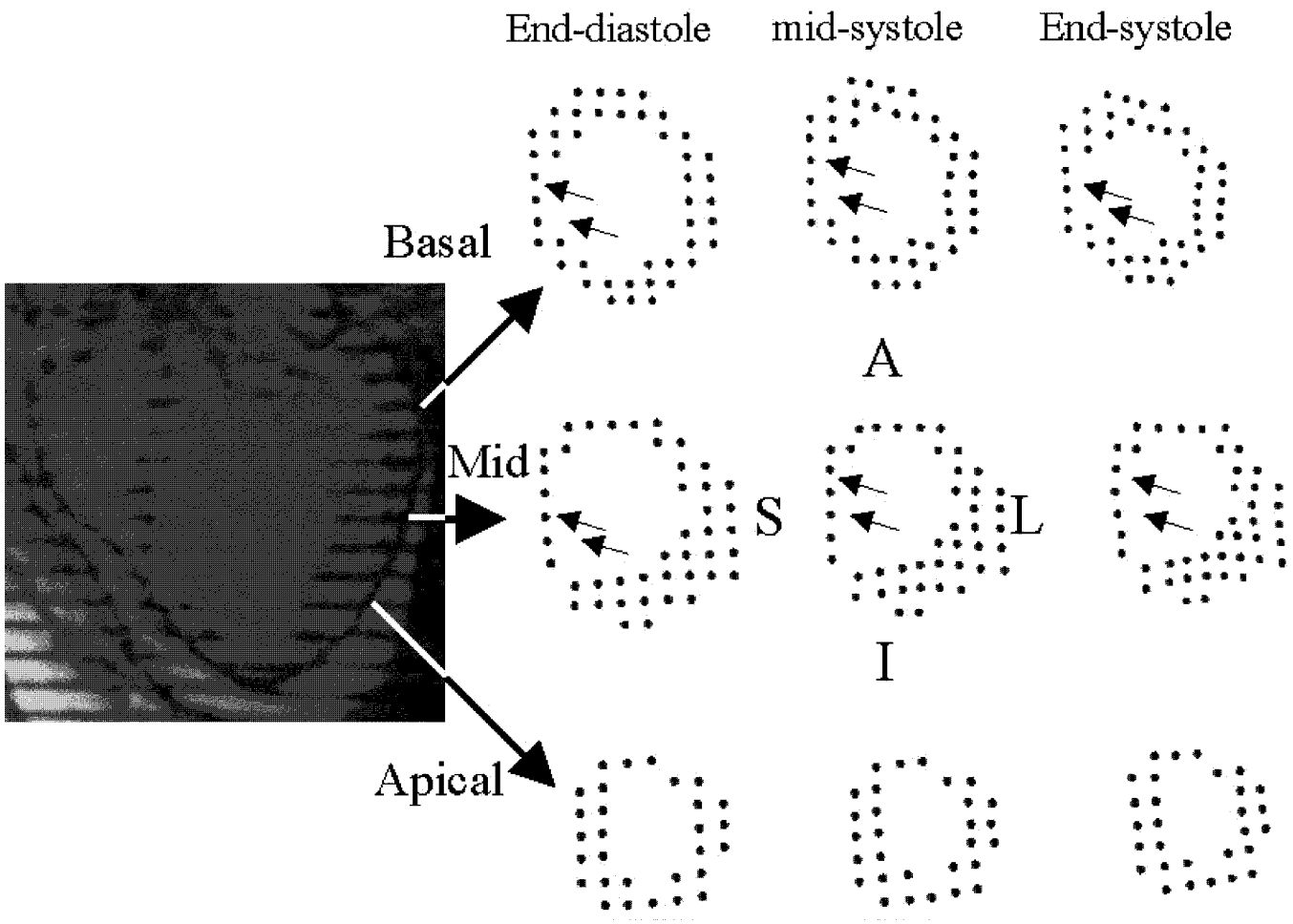

Fig. 13. MRI of the left-ventricular long-axis view with tissue-tagging (left) in a patient with a history of an antero-septal myocardial infarction. The antero-septal wall (arrows) shows no motion of the beads during the systolic phase of the cardiac cycle (end-diastole to mid-systole to end-systole), reflecting akinesis of these segments, compatible with myocardial infarction (right). Note that the location of beads at end-diastole correspond to short-axis slice positions as shown on the long-axis image.

entations including SA and LA images [1]. The parameters of the motion model, referred to as k-parameters, and the transformations to which they correspond are stated in Table I.

For generating MR images, an imaging plane intersecting the geometric model is selected, and tagged spin-echo imaging equations are applied for simulating the *in-vivo* imaging process. Fig. 6 displays an undeformed 3-D model (with all the k-parameters identical to zero) and simulated tagged images corresponding roughly to the middle of the LV. Application of deformations to the model result in representative images as shown in Fig. 7. The imaging and geometric parameters of the model for this figure are stated in Table II.

The correspondence of LA tag planes and SA image slices as well as one set of SA tag planes and the LA image slices in the undeformed state was ensured by computing from [18, Eq. (11)] in each case the exact location of the tag plane intersecting the 3-D model and subsequently choosing the location of the image slice to be identical to this position. The SA image planes are located at: $z = -1.57$, -0.785, 0, 0.785, 1.57, 2.355, 3.14, 3.925 (all locations in cm) which coincide with position of LA tag planes in the undeformed state. The LA image planes are located at: $y = -2.355$, -1.57, -0.785, 0, 0.785, 1.57, 2.355 (all locations in cm) which coincide with position of one set of SA tag planes. Therefore, there are eight SA slices and 7 LA slices. The slice separation as well as the tag separations in SA and LA images were 0.785 cm.

To compute a figure of merit for the algorithm, the root-mean-square (rms) error between theoretical intersections, $\vec{P}_i^t$ and the computed intersections, $\vec{P}_i^c$, are calculated

$$\text{rms} = \sqrt{\frac{1}{N}\sum_{i=1}^{N}\left|\vec{P}_i^t - \vec{P}_i^c\right|^2} \tag{7}$$

where the sum is over all myocardial beads across all spatial slices for a given volumetric time frame.

Because the accuracy of the intersection calculations are affected by both the tag line detection/tracing procedure as well as tag spacings, in order to remove the effect of errors in tag line detection/tracing, we use the theoretical tag line locations (known from the simulator parameters) for validating the computed intersections for each of the six image collection time points for k_3, k_7, and k_9 sequences. The 3-D rms error curves are shown in Fig. 8. The plots indicates that these errors which are solely due to numerical optimization and round-off errors

in computing the location of myocardial beads are truly negligible (on the order of 0.01 cm). Fig. 9 displays how the rms error varies with the tag spacing under tag line detection/manual correction for k_1 and k_2 sequences.[1] The error curves in this case clearly indicate larger errors than those in Fig. 8. However, note that when tag spacing is reduced by half, the rms error is reduced by half or by third, for the parameters k_1 and k_2 respectively. Fig. 10 shows the rms error for the entire cardiac cycle when all the 13 k parameters are concurrently varied (see Table III). The time evolution of the 13 k parameters are as those reported in [6] and [18], representing canonical deformations of an *in-vivo* canine LV. As a visual example, Fig. 11 shows intersections computed for the k_2 simulated images from frame 0 to frame 5. The algorithm was also tested on a normal human image sequence which included 17 slices and 19 frames (17×19 images) yielding temporal position of around 250 beads over the heart cycle. In a movie of these beads, the 3-D motion of individual SPAMM points of the myocardium is clearly apparent. Fig. 12 displays results of the intersection computation for few of the short-axis slices. Fig. 13 shows application of the algorithm to images collected from a patient with an old, healed, antero-septal myocardial infarction.

V. Conclusion

In conclusion, we have described efficient methods for encoding, visualization, and tracking of 3-D myocardial beads in the heart from two sets of orthogonal tagged MR views. We have argued that in comparison to other forms of tag representation, use of B-splines has several advantages, including immediate generation of tag surfaces, subpixel accuracy for tag plane localization and parametric continuity, as well as the need to only assign the location of few control points in order to determine the location of a complete tag surface.

References

[1] A. Amini, Y. Chen, R. Curwen, V. Mani, and J. Sun, "Coupled B-snake grids and constrained thin-plate splines for analysis of 2-D tissue deformations from tagged MRI," *IEEE Trans. Med. Imag.*, vol. 17, pp. 344–356, Mar. 1998.

[1]For k_3, k_7, and k_9 image sequences, it is possible to obtain the exact location of the B-Snake grid control point locations (and consequently 3-D coordinates of tag curves) for all time points by directly applying the simulator deformation matrix [18] to the coordinates of the control points in the undeformed state. However, due to the nonlinear nature of the k_1 and k_2 (radially dependent compression and torsion) transformations, for the k_1 and k_2 parameters, this cannot be achieved.

[2] A. A. Amini, R. W. Curwen, and J. C. Gore, "Snakes and splines for tracking nonrigid heart motion," in *Proc. Eur. Conf. Computer Vision*, Apr. 1996, pp. 251–261.

[3] A. A. Amini *et al.*, "Energy-minimizing deformable grids for tracking tagged MR cardiac images," in *Comput. Cardiol.*, 1992, pp. 651–654.

[4] A. A. Amini *et al.*, "MR physics-based snake tracking and dense deformations from tagged MR cardiac images (oral presentation)," presented at the AAAI Symp. Applications of Computer Vision to Medical Image Processing, Stanford, CA, Mar. 1994.

[5] A. A. Amini, P. Radeva, and D. Li, "Measurement of 3D motion of myocardial material points from explicit B-surface reconstruction of tagged data," presented at the Medical Image Computing and Computer-Assisted Interventions-MICCAI'98, Cambridge, MA, Oct. 1998.

[6] T. Arts, W. Hunter, A. Douglas, A. Muijtjens, and R. Reneman, "Description of the deformation of the left ventricle by a kinematic model," *J. Biomech.*, vol. 25, no. 10, pp. 1119–1127, 1992.

[7] F. Bookstein, "Principal warps: Thin-plate splines and the decomposition of deformations," *IEEE Trans. Pattern Anal. Machine Intell.*, vol. 11, pp. 567–585, June 1989.

[8] M. Moulton *et al.*, "Spline surface interpolation for calculating 3-D ventricular strains from MRI tissue tagging," *Amer. J. Physiol.*, vol. 270, pp. H281–H297, 1996.

[9] S. Gupta and J. Prince, "On variable brightness optical flow for tagged MRI," in *Proc.Information Processing in Medical Imaging (IPMI)*, 1995, pp. 323–334.

[10] M. Guttman, J. Prince, and E. McVeigh, "Tag and contour detection in tagged MR images of the left ventricle," *IEEE Trans. Med. Imag.*, vol. 13, no. 1, pp. 74–88, 1994.

[11] J. Huang, D. Abendschein, V. Davila-Roman, and A. Amini, "Spatio-temporal tracking of myocardial deformations with a 4D B-spline model from tagged MRI," *IEEE Trans. Med. Imag.*, vol. 18, pp. 957–972, Oct. 1999.

[12] W. Kerwin and J. Prince, "Generating 3-D cardiac material markers using tagged MRI," in *Proc. Information Processing in Medical Imaging (IPMI)*, 1997, pp. 313–326.

[13] A. Klein, F. Lee, and A. Amini, "Quantitative coronary angiography with deformable spline models," in *IEEE Trans. Med. Imag.*, Oct. 1997, vol. 16, pp. 468–482.

[14] S. Menet, P. Saint-Marc, and G. Medioni, "B-snakes: Implementation and application to stereo," in *Proc. DARPA Image Understanding Workshop*, Pittsburgh, PA, Sept. 1990, pp. 720–726.

[15] M. E. Mortenson, *Geometric Modeling*. New York: Wiley, 1985.

[16] J. Park, D. Metaxas, and L. Axel, "Volumetric deformable models with parameter functions: A new approach to the 3D motion analysis of the LV from MRI-SPAMM," in *Proc. Int. Conf. Computer Vision*, 1995, pp. 700–705.

[17] P. Radeva, A. Amini, and J. Huang, "Deformable B-solids and implicit snakes for 3D localization and tracking of SPAMM MRI data," *Comput. Vis. Image Understanding*, vol. 66, no. 2, pp. 163–178, May 1997.

[18] E. Waks, J. Prince, and A. Douglas, "Cardiac motion simulator for tagged MRI," in *Proc. Mathematical Methods in Biomedical Image Analysis*, 1996, pp. 182–191.

[19] A. Young, D. Kraitchman, L. Dougherty, and L. Axel, "Tracking and finite element analysis of stripe deformation in magnetic resonance tagging," *IEEE Trans. Med. Imag.*, vol. 14, no. 3, pp. 413–421, Sept. 1995.

[20] E. Zerhouni, D. Parish, W. Rogers, A. Yang, and E. Shapiro, "Human heart: Tagging with MR imaging—A method for noninvasive assessment of myocardial motion," *Radiology*, vol. 169, pp. 59–63, 1988.